Dissertation

High Order Finite Element S_N Thermal Radiation Transport on Meshes with Curved Surfaces

Douglas N. Woods

11 June 2018

TABLE OF CONTENTS

LIST OF FIGURES

LIST OF TABLES

1 Introduction

There are several applications for the thermal radiation transport (TRT) equation for nuclear fusion. Two of which include astrophysics such as stars or supernovae [1], and inertial confinement fusion such as the National Ignition Facility[1] (NIF). Nuclear fusion occurs in the high energy density physics (HEDP) regime where mass and energy densities of a material are very high [2, 1]. Since material temperatures are very high, materials emit black body radiation in tremendous quantities. This thermal radiation field deposits energy back to the material influencing the material internal energy, temperature, and density. The radiation field can exchange enough momentum with the material that it directly affects the fluid motion [1]. Radiation transport and material absorption and emission are interdependent mechanisms that must be modeled simultaneously to obtain an energy distribution throughout the material. The material may also be exposed to additional hydrodynamic forces that change pressures, introduce density fluctuations, and cause fluid motion. In turn, the motion and energy density of the fluid affects the location and quantity of radiation emission. This complicated system of thermal radiation transport with hydrodynamics is studied in radiation hydrodynamics. While all of the forces in these HEDP systems are important, we can study some of the effects independently. For instance, we study hydrodynamics separately from TRT.

The staggered grid hydrodynamics (SGH) approach is considered a traditional approach that uses the finite difference or finite volume methods, and has to compensate for calculating the spatial gradients, which are highly dependent on the mesh resolution [3]. The finite element method (FEM) has been employed, approximating the thermodynamic variables as piecewise constant and the kinematic variables as linear continuous[4], and higher order finite elements [5].

---

[1]`https://lasers.llnl.gov`

Lawrence Livermore National Laboratory (LLNL) is developing a hydrodynamics code called BLAST.[2] [3]. It solves the Euler equations using a general finite element method (FEM) on meshes with curved surfaces for the conservation of mass, energy, and momentum of a fluid [5]. Novel features include: higher order elements to represent the thermodynamic and kinematic variables, and meshes with curved surfaces. Compared to SGH, Dobrev et al. [5] demonstrated their method can more accurately model flow geometry, symmetry of radial flow, and an increased resolution of a shock front saying their method has the ability to model the shock within a single mesh element. These improvements have reduced some of the numerical errors that have been exhibited by previous methods.

BLAST utilizes MFEM [6], a general finite element library also being developed at LLNL, to spatially discretize using the high order FEM on meshes with curved surfaces. This proposed TRT research could be combined with a hydrodynamics code such as BLAST to develop a radiation hydrodynamics package to better model HEDP problems such as those produced during inertial confinement fusion at the NIF. The integrated radiation hydrodynamics code will need each physics package to numerically solve the same physical problem and communicate between packages. Hence, it is advantageous to utilize the same general finite element library when considering the integration of code packages.

This chapter introduces TRT and establishes our motivation for using the proposed methods. In Section 1.1, we give a brief introduction to the TRT equations and nomenclature. In Section 1.2, we describe various discretization methods used to solve the TRT equations. In Section 1.3, we describe the diffusion limit and it's application to optically thick problems found in HEDP regimes. Finally, in Section 1.4, we outline the remained of this research proposal.

---

[2]https://computation.llnl.gov/project/blast/

1.1 Thermal Radiation Transport

High energy density material absorbs and emits radiation. The property of interest is the energy density and/or temperature of the material. We introduce the radiation intensity

$$I\left(\boldsymbol{r}, \boldsymbol{\Omega}, \nu, t\right) = h\nu f\left(\boldsymbol{r}, \boldsymbol{\Omega}, \nu, t\right) \tag{1}$$

which describes the energy at position $\boldsymbol{r}$, traveling in direction $\boldsymbol{\Omega}$, with frequency $\nu\,[\mathrm{s}^{-1}]$, at time t, where $f\,[\mathrm{cm}^{-2} \cdot \mathrm{s}^{-1} \cdot \mathrm{ster}^{-1}]$ is the equivalent to the photon density, $h = 6.26 \times 10^{-34}\ \mathrm{J \cdot s}$ is the Planck constant, and $\epsilon\,[\mathrm{J}] = h\nu$ is the photon energy with frequency ν. The TRT equations can then be written [7]

$$\frac{1}{c}\frac{\partial I}{\partial t} + \boldsymbol{\Omega} \cdot \boldsymbol{\nabla} I + \sigma_t I = \frac{\sigma_s}{4\pi}\int_{4\pi} I d\Omega' + \sigma_a B + S_0 \tag{2a}$$

$$\frac{\partial u_m}{\partial t} = -\int_0^\infty \int_{4\pi} c\sigma_a\left(B - I\right) d\Omega' d\nu + Q_m \tag{2b}$$

where $c = 3.00 \times 10^8\ \mathrm{m \cdot s^{-1}}$ is the speed of light in a vacuum, $\sigma_t\,[\mathrm{cm}^{-1}] = \sigma_s + \sigma_a$ is the total opacity, $\sigma_s\,[\mathrm{cm}^{-1}]$ is the scattering opacity, $\sigma_a\,[\mathrm{cm}^{-1}]$ is the absorption opacity, $B\,[\mathrm{J \cdot cm^{-1} \cdot s^{-1}}]$ is Planck's function as a function of material temperature and photon frequency, $S_0\,[\mathrm{J \cdot cm^{-2} \cdot s^{-1}}]$ is an external source of photon frequency, $u_m\,[\mathrm{J}]$ is the energy density of the material, and $Q_m\,[\mathrm{J \cdot s^{-1}}]$ is an external material heat source.

Equations 2 are functions of seven variables: three in space ($\boldsymbol{r}$), two in direction of travel ($\boldsymbol{\Omega}$), frequency (ν), and time (t). Equation 2a describes the intensity balance of losses and gains. Particularly, $\partial I/\partial t$ describes the change in intensity over time, $\boldsymbol{\Omega} \cdot \boldsymbol{\nabla} I$ is the streaming term, $\sigma_t I$ is the absorption term, $\sigma_s/4\pi \int_{4\pi} I d\Omega'$ is the scattering term, $\sigma_a B$ is the emission term, and S_0 is an arbitrary volumetric source.

Equation 2b describes the material energy balance. Particularly, $\partial u_m/\partial t$ describes the change in energy over time, $\int d\nu \int d\Omega' c\sigma_a B$ is the power loss due to radiation emission, $\int d\nu \int d\Omega' c\sigma_a I$ is the power gain due to radiation absorption, and Q_m is an external material heat source. The desired solution to TRT applications involves both the distribution of the radiation field and the material energy and temperature distributions.

There are only a few specific cases where the TRT equations can be solved exactly. Problems of interest typically fall outside of this subset and numerical methods must be employed to attain a solution. There are two general categories of methods used to solve this equation: Monte Carlo methods and deterministic methods.

Monte Carlo methods take a statistical approach. A single photon is followed from its birth through its "random walk" through the problem domain until it is either absorbed or escapes the domain. If enough photons are simulated, a statistically significant conclusion can be drawn about the photon density in a region of interest. This is very accurate but also computationally demanding because of the large number of photons required to be simulated.

Alternatively, deterministic methods approach the problem by discretizing the TRT equations in each of their dependent variables and solving a nonlinear algebraic system of equations. These methods are generally faster than Monte Carlo methods but involve discretization or truncation errors. However, employing certain discretizations can reduce the impact of these errors.

1.2   Discretization

Physically, 3-dimensional space is continuous: a photon could exist at any one of an infinite number of locations. Numerically, it is impossible to compute a solution at an infinite number of locations so we discretize the spatial domain into a small

subset of locations. Similarly, a photon can travel in an infinite number of directions so we approximate it traveling in only a few. Discretizing the direction of travel by using the discrete ordinates (S_N) method [8] is common. Photons may behave or interact with material differently at different frequencies. We approximate an infinite number of photon frequencies by grouping them into a finite number of groups. If a problem evolves through time, we discretize the time continuum with small discrete steps through time.

There are several methods of spatial discretization that appear in the transport community. Among the most common are characteristic methods [9], finite difference methods [10], finite volume methods, and finite element methods (FEMs) [10]. Typically, the problem domain is divided to a larger number of smaller domains. The equations are then numerically solved on each of these smaller regions where the solution is likely less varying when compared to the entire problem. The FEM has been favored for it's ability to perform in the thick diffusion limit [11] (discussed in Sections 1.3 and ??). Thus, this research uses the FEM in which the solution is approximated to have a functional form within each mesh element. More discussion of various discretization methods can be found in Lewis and Miller [10].

Additionally, these TRT problems are solved in each of Cartesian, cylindrical (R-Z), and spherical coordinates. The present research is concerned with Cartesian and R-Z geometries. Difficulties arise in R-Z geometry because of the introduction of angular derivatives. While a photon travels in a straight line in direction $\boldsymbol{\Omega}$, the cosines of the angles relative to the coordinate axes change as the r and z coordinates change.

1.3 Diffusion Limit

HEDP problems are examples of scenarios where a photon has a very small mean free path compared to the size of the spatial mesh. This happens when the total opacity σ_t becomes very large. These problems are called "optically thick". Often, a simplified version of the TRT equations is considered when determining the performance of a discretization method in the diffusion limit: the uncoupled, steady-state, radiation transport equation (RTE)

$$\mathbf{\Omega} \cdot \mathbf{\nabla} I + \sigma_t I = \frac{\sigma_s}{4\pi} \int_{4\pi} I d\Omega' + S_0 \tag{3}$$

This simplified equation must behave well in the optically thick regime if we are to expect the same from the more complex TRT equations. The RTE behaves well when the spatial mesh is optically thin. But we can assess the behavior of Equation 3 as the problem becomes increasingly optically thick by performing an asymptotic analysis. Specifically, if a small factor ε is used to scale the physical processes of Equation 3,

$$\mathbf{\Omega} \cdot \mathbf{\nabla} I + \frac{\sigma_t}{\varepsilon} I = \frac{1}{4\pi} \left(\frac{\sigma_t}{\varepsilon} - \varepsilon \sigma_a \right) \int_{4\pi} I d\Omega' + \varepsilon S_0 \tag{4}$$

then as $\varepsilon \to 0$ the mean free path $\Lambda = \varepsilon/\sigma_t \to 0$. In this limit, the problem is said to be optically thick and diffusive. It can be shown [12] that this scaled analytic RTE limits to the analytic radiation diffusion equation to $O(\varepsilon^2)$. Thus, problems that are typically solved by using the radiation diffusion equation (because they are highly diffusive) can also be solved using the RTE.

The source iteration (SI) method [10] is commonly employed to solve the dis-

cretized RTE. The algorithm

$$\mathbf{\Omega} \cdot \nabla I^{(l+1)} + \sigma_t I^{(l+1)} = \frac{1}{4\pi} \sigma_s E^{(l)} + S_0 \tag{5a}$$

$$E^{(l+1)} = \sum_m w_m I_m^{(l+1)} \tag{5b}$$

describes the calculation of the intensity using the lagged energy density followed by an update to the energy density using the angular quadrature weights w_m, where the energy density is

$$E\left(\mathbf{r}, \nu, t\right) = \int_{4\pi} I\left(\mathbf{r}, \mathbf{\Omega}, \nu, t\right) d\Omega \tag{6}$$

The RTE can converge arbitrarily slowly in these optically thick regimes [13]. To speed up the SI, one option is to refine the mesh until the optical thickness of a typical mesh cell is on the order of a mean-free-path to, effectively, solve an optically thin problem in each mesh zone. This option is not very efficient because it can introduce a large number of degrees of freedom to the problem, thereby increasing the solver time. Alternatively, acceleration techniques can be applied to the SI to compensate for slow convergence. Diffusion synthetic acceleration is commonly used to accelerate the source iteration and is discussed in more detail below.

1.4 Outline

The remainder of this paper is outlined as follows.

2 High Order DFEM

This section describes the methods to be carried out to accomplish the proposed research. We also consider some potential issues that we may encounter with some initial thoughts about mitigation.

2.1 Basis Functions

3   Meshes with Curved Surfaces

3.1   Transformation

4 Diffusion Synthetic Acceleration

This section describes the methods to be carried out to accomplish the proposed research. We also consider some potential issues that we may encounter with some initial thoughts about mitigation.

4.1 Modified Interior Penalty DSA

4.1.1 Methodology

4.1.2 Fourier Analysis

4.1.3 Results

4.1.4 As a Preconditioner

4.2 MIP DSA with Robin Boundary Conditions

The diffusion synthetic acceleration (DSA) algorithm first solves the RTE, called a "transport sweep", followed by a diffusion solve for each source iteration. The RTE solve is performed exactly as before (Eqs. 5) with notation changing to indicate a "half step":

$$\boldsymbol{\Omega} \cdot \boldsymbol{\nabla} I^{(l+1/2)} + \sigma_t I^{(l+1/2)} = \sigma_s E^{(l)} + S_0 \tag{7a}$$

$$E^{(l+1/2)} = \sum_{m=1}^{M} w_m \; I_m^{(l+1/2)} \left(\boldsymbol{r}, \boldsymbol{\Omega} \right) \tag{7b}$$

(Recall the energy density E defined by Equation 6.) Next, we solve the diffusion equation with a modified source term utilizing the half step and previous iteration RTE solutions.

$$-\boldsymbol{\nabla} \cdot D\boldsymbol{\nabla}\phi^{(I+1/2)} + \sigma_a \phi^{(l+1/2)} = \sigma_s \left(E^{(l+1/2)} - E^{(l)} \right) \tag{7c}$$

The diffusion solution, $\phi^{(l+1/2)}$, becomes the correction factor at the half step. This correction factor is added to the energy density at the half step to complete the full DSA iteration.

$$E^{(l+1)} = E^{(l+1/2)} + \phi^{(l+1/2)} \tag{7d}$$

This iterative process continues until the convergence criteria

$$\left\| E^{(l+1)} - E^{(l)} \right\|_\infty < \varepsilon_{\text{conv}} \left(1 - \rho \right) \left\| E^{l+1} \right\|_\infty, \tag{8}$$

is met, where $\varepsilon_{\text{conv}}$ is a small number.

Wang and Ragusa [14] proposed the modified interior penalty (MIP) equations for discretizing the DSA equation using the DGFEM:

$$
\begin{aligned}
b_{MIP}\left(\phi, w \right) = {} & \left(\sigma_a \phi, w \right)_\mathbb{V} + \left(D\boldsymbol{\nabla}\phi, \boldsymbol{\nabla}w \right)_\mathbb{V} \\
& + \left(\kappa_e [\![\phi]\!], [\![w]\!] \right)_{\partial\mathbb{V}^i} + \left([\![\phi]\!], \{\!\{ D\partial_n w \}\!\} \right)_{\partial\mathbb{V}^i} + \left(\{\!\{ D\partial_n \phi \}\!\}, [\![w]\!] \right)_{\partial\mathbb{V}^i} \\
& + \left(\kappa_e \phi, w \right)_{\partial\mathbb{V}^d} - \frac{1}{2} \left(\phi, D\partial_n w \right)_{\partial\mathbb{V}^d} - \frac{1}{2} \left(D\partial_n \phi, w \right)_{\partial\mathbb{V}^d} \tag{9}
\end{aligned}
$$

and

$$l_{MIP}\left(w \right) = \left(Q_0, w \right)_\mathbb{V} \tag{10}$$

where b_{MIP} is the bilinear form, l_{MIP} is the linear form, w is the weight/test function, $\mathbb{V}$ denotes the element volume, $\partial\mathbb{V}^i$ is the internal edges, $\partial\mathbb{V}^d$ is on the problem boundary, ∂_n is the partial derivative perpendicular to the edge (i.e. $\boldsymbol{\nabla} \cdot \hat{n}$). The following definitions accompany Equations 9 and 10.

$$\llbracket \phi \rrbracket = \phi^+ - \phi^- \tag{11}$$

$$\{\!\{\phi\}\!\} = \frac{(\phi^+ + \phi^-)}{2} \tag{12}$$

$$Q_0 = \sigma_s \left(E^{(l+1/2)} - E^{(l)} \right) \tag{13}$$

$$\kappa_e^{IP} = \begin{cases} \frac{c(p^+)}{2}\frac{D^+}{h_\perp^+} + \frac{c(p^-)}{2}\frac{D^-}{h_\perp^-}, & \text{on interior edges (i.e., } \boldsymbol{r} \in E_h^i) \\[2ex] c\,(p)\,\frac{D}{h_\perp}, & \text{on boundary edges } \left(\text{i.e., } \boldsymbol{r} \in \partial D^d\right) \end{cases} \tag{14}$$

$$\kappa_e = \max\left(\kappa_e^{IP}, \frac{1}{4} \right) \tag{15}$$

$$c\,(p) = C p\,(p+1) \tag{16}$$

where C is a an arbitrary constant, $D^\pm$ is the diffusion coefficient, $\phi^\pm$ is the scalar flux, $p^\pm$ is the order of finite elements, and $h_\perp^\pm$ is the perpendicular length of the cell, where the $\pm$ denotes either side of an element boundary. Equation 15 is a "switch" between two methods (interior penalty and diffusion conforming form), one of which is stable for optically thin regions and the other for optically thick regions. Wang and Ragusa [14] used $C = 2$ and Turcksin and Ragusa [15] used $C = 4$.

4.2.1 Zero Incident Current

Kanschat [16] shows that Equations 9 and 10 employ Nitsche's method for "a fully conforming method of treating Dirichlet boundary values." The boundary terms $\left(\partial \mathbb{V}^d\right)$ in this form are homogeneous Dirichlet boundary conditions. The result is that the DSA correction for the energy density at the problem boundaries is zero, so the energy density is only updated by the RTE solution. That is, the DSA correction only accelerates the interior solution. Consequently, the energy densities on the problem boundary is only subjected to the RTE solution source iterations.

Instead, a DSA update equation should incorporate Robin boundary conditions (zero incident partial current) on the boundaries,

$$\boldsymbol{J}_- = 0 = \frac{1}{4}\phi + \frac{1}{2}D\boldsymbol{\nabla}\phi \cdot \hat{n}, \tag{17}$$

$$-\frac{1}{2}\phi = D\boldsymbol{\nabla}\phi \cdot \hat{n}, \tag{18}$$

thereby allowing a correction of the boundary energy densities. This boundary condition requires modification of Equation 9. Three implementaion methods are proposed here. Method 1 substitutes Equation 18 into Equation 9:

$$b_{MIP,1}\left(\phi, w\right) = (\sigma_a\phi, w)_{\mathbb{V}} + (D\boldsymbol{\nabla}\phi, \boldsymbol{\nabla}w)_{\mathbb{V}}$$

$$+ (\kappa_e[\![\phi]\!], [\![w]\!])_{\partial\mathbb{V}^i} + ([\![\phi]\!], \{\!\{D\partial_n w\}\!\})_{\partial\mathbb{V}^i} + (\{\!\{D\partial_n\phi\}\!\}, [\![w]\!])_{\partial\mathbb{V}^i}$$

$$+ (\kappa_e\phi, w)_{\partial\mathbb{V}^d} - \frac{1}{2}(\phi, D\partial_n w)_{\partial\mathbb{V}^d} + \frac{1}{4}(\phi, w)_{\partial\mathbb{V}^d} \tag{19}$$

Method 2 is very similar to Method 1 with one term removed:

$$b_{MIP,2}\left(\phi, w\right) = (\sigma_a\phi, w)_{\mathbb{V}} + (D\boldsymbol{\nabla}\phi, \boldsymbol{\nabla}w)_{\mathbb{V}}$$

$$+ (\kappa_e[\![\phi]\!], [\![w]\!])_{\partial\mathbb{V}^i} + ([\![\phi]\!], \{\!\{D\partial_n w\}\!\})_{\partial\mathbb{V}^i} + (\{\!\{D\partial_n\phi\}\!\}, [\![w]\!])_{\partial\mathbb{V}^i}$$

$$+ (\kappa_e\phi, w)_{\partial\mathbb{V}^d} + \frac{1}{4}(\phi, w)_{\partial\mathbb{V}^d} \tag{20}$$

Method 3 stems from a different approach. After performing the integration by parts on the diffusion term,

$$-(\boldsymbol{\nabla} \cdot D\boldsymbol{\nabla}\phi, w)_{\mathbb{V}} = (D\boldsymbol{\nabla}\phi, \boldsymbol{\nabla}w)_{\mathbb{V}} - (D\boldsymbol{\nabla}\phi \cdot \hat{n}, w)_{\partial\mathbb{V}^i} - (D\boldsymbol{\nabla}\phi \cdot \hat{n}, w)_{\partial\mathbb{V}^d}, \tag{21}$$

we employ Equation 18:

$$-\left(\boldsymbol{\nabla} \cdot D\boldsymbol{\nabla}\phi, w\right)_{\mathbb{V}} = \left(D\boldsymbol{\nabla}\phi, \boldsymbol{\nabla}w\right)_{\mathbb{V}} - \left(D\boldsymbol{\nabla}\phi \cdot \hat{n}, w\right)_{\partial\mathbb{V}^i} + \frac{1}{2}\left(\phi, w\right)_{\partial\mathbb{V}^d} \qquad (22)$$

Thus, Method 3 is

$$b_{MIP,3}\left(\phi, w\right) = \left(\sigma_a\phi, w\right)_{\mathbb{V}} + \left(D\boldsymbol{\nabla}\phi, \boldsymbol{\nabla}w\right)_{\mathbb{V}}$$

$$+ \left(\kappa_e[\![\phi]\!], [\![w]\!]\right)_{\partial\mathbb{V}^i} + \left([\![\phi]\!], \{\!\{D\partial_n w\}\!\}\right)_{\partial\mathbb{V}^i} + \left(\{\!\{D\partial_n\phi\}\!\}, [\![w]\!]\right)_{\partial\mathbb{V}^i}$$

$$+ \frac{1}{2}\left(\phi, w\right)_{\partial\mathbb{V}^d} \quad (23)$$

We will implement these three methods and investigate their impact on the solution behavior. We will first solve a 1-D analytic diffusion equation problem with zero incident current boundary conditions to evaluate our implementation.

4.2.2 Fourier Analysis

4.2.3 Results

4.2.4 As a Preconditioner

5   *R-Z* Geometry

This section describes the methods to be carried out to accomplish the proposed research. We also consider some potential issues that we may encounter with some initial thoughts about mitigation.

5.1   DFEM

The RTE in *R-Z* geometry is [10]

$$
\frac{\mu}{r}\frac{\partial}{\partial r}rI\left(r,z,\boldsymbol{\Omega}\right) - \frac{1}{r}\frac{\partial}{\partial \omega}\eta I\left(r,z,\boldsymbol{\Omega}\right) + \xi\frac{\partial}{\partial z}I\left(r,z,\boldsymbol{\Omega}\right) + \sigma_t\left(r,z\right)I\left(r,z,\boldsymbol{\Omega}\right)
$$
$$
= \frac{1}{4\pi}\int_{4\pi}\sigma_s\left(r,z\right)I\left(r,z,\boldsymbol{\Omega}'\right)d\Omega' + S_0\left(r,z,\boldsymbol{\Omega}\right) \quad (24)
$$

where I is the intensity, σ_t is the total opacity, σ_s is the scattering opacity, S_0 is an arbitrary source, and ω is defined in the cylindrical coordinate system shown in Figure 1. The direction of travel is defined by

$$
\mu \equiv \boldsymbol{\Omega}\cdot\hat{e}_r = \sqrt{1-\xi^2}\cos\omega = \sin(\theta)\cos(\omega), \quad (25)
$$

$$
\eta \equiv \boldsymbol{\Omega}\cdot\hat{e}_\theta = \sqrt{1-\xi^2}\sin\omega = \sin(\theta)\sin(\omega), \quad (26)
$$

$$
\xi \equiv \boldsymbol{\Omega}\cdot\hat{e}_z = \cos(\theta). \quad (27)
$$

Discretizing Equation 24 with a level-symmetric angular quadrature results in

$$
\frac{\mu_{m,n}}{r}\frac{\partial}{\partial r}rI_{m,n}\left(r,z\right) - \frac{1}{r}\frac{\partial}{\partial \omega}\eta_{m,n}I_{m,n}\left(r,z\right) + \xi_n\frac{\partial}{\partial z}I_{m,n}\left(r,z\right) + \sigma_t\left(r,z\right)I_{m,n}\left(r,z\right)
$$
$$
= \frac{1}{4\pi}\int_{4\pi}\sigma_s\left(r,z\right)I\left(r,z,\boldsymbol{\Omega}'\right)d\Omega' + S_0\left(r,z,\boldsymbol{\Omega}\right) \quad (28)
$$

for direction $\boldsymbol{\Omega}_{m,n}$, where index n describes a level of quadrature with constant ξ and the m index denotes the quadrature point on that level. Lewis and Miller [10]
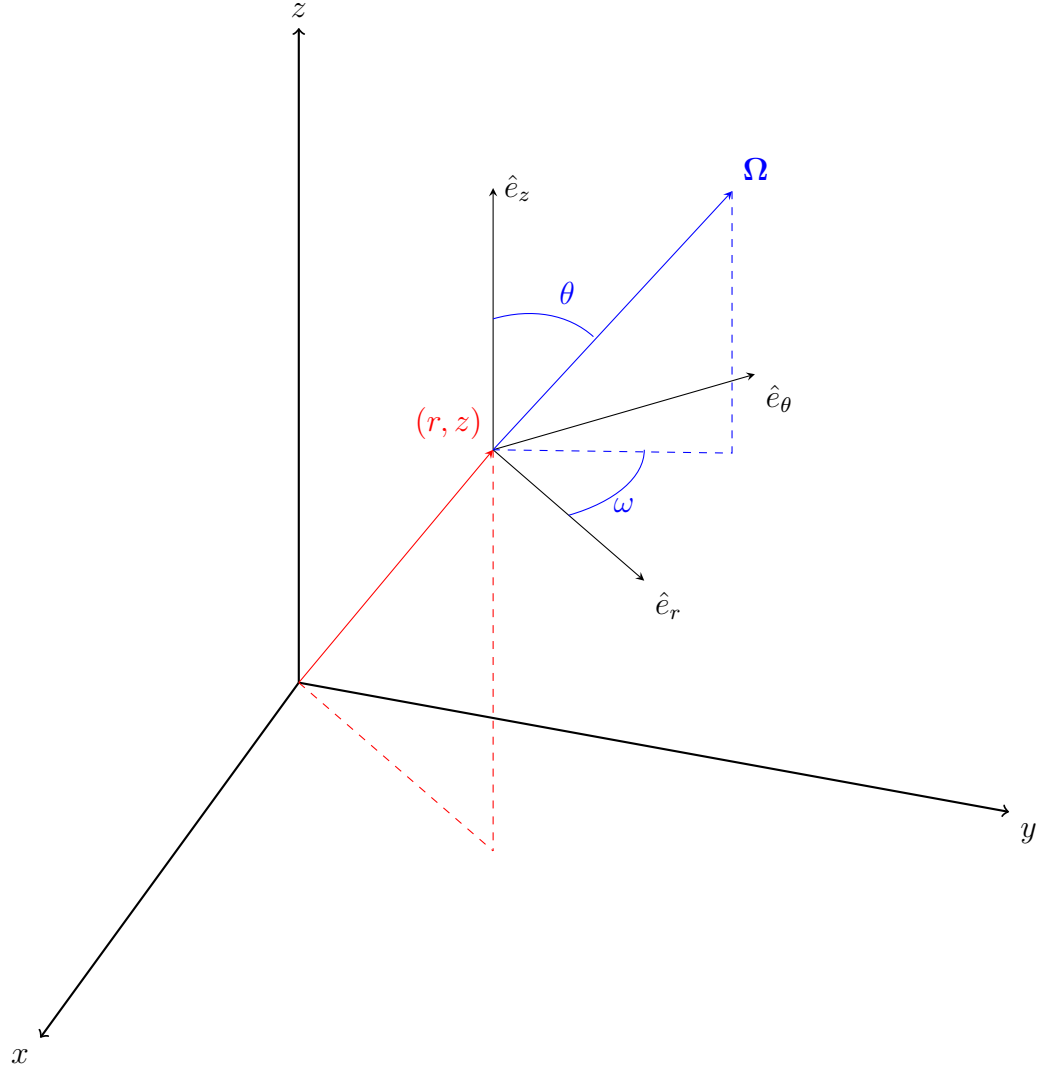
Figure 1: Cylindrical coordinate system.

describes an approximation for the partial derivative of the intensity with respect to ω:

$$-\frac{1}{r}\frac{\partial}{\partial\omega}\eta_{m,n}I_{m,n}\left(r,z\right) = \frac{\alpha_{m+1/2}^{n}I_{m+1/2,}(r,z) - \alpha_{m-1/2}^{n}I_{m-1/2,n}(r,z)}{rw_{m,n}} \tag{29}$$

where $\alpha_{m+1/2}^{n}$ and $\alpha_{m-1/2}^{n}$ are angular differencing coefficients, and $w_{m,n}$ is the angular

quadrature weight. We substitute this into Equation 28,

$$\frac{\mu_{m,n}}{r}\frac{\partial}{\partial r}rI_{m,n}\left(r,z\right)+\frac{\alpha^n_{m+1/2}I_{m+1/2,n}(r,z)-\alpha^n_{m-1/2}I_{m-1/2,n}(r,z)}{rw_{m,n}}$$

$$+\xi_n\frac{\partial}{\partial z}I_{m,n}\left(r,z\right)+\sigma_t\left(r,z\right)I_{m,n}\left(r,z\right)$$

$$=\frac{1}{4\pi}\int_{4\pi}\sigma_s\left(r,z\right)I\left(r,z,\boldsymbol{\Omega}'\right)d\Omega'+\frac{1}{4\pi}S_0\left(r,z\right)\quad(30)$$

Here, we pause to notice that there are similarities and differences between our Cartesian discretization. The absorption term, axial derivative term, and right-hand-side are the same in both coordinate systems. The differences arise in the radial and angular derivative terms. After multiplying through by the radius r, the radial derivative term has a factor of r inside the derivative. The angular derivative term is also new and does not resemble a mass matrix so MFEM will require additional modification.

Requiring Equation 30 to satisfy the uniform infinite medium solution results in the condition,

$$\alpha^n_{m+1/2}=\alpha^n_{m-1/2}-\mu_{m,n}w_{m,n}\quad(31)$$

If $\alpha^n_{1/2}$ is known, then the remaining coefficients are uniquely determined. To find $\alpha^n_{1/2}$, we require that Equation 30 satisfy the conservation equation (Eq. 24). Given a quadrature set with an even number of $\mu_{m,n}$ values, setting $\alpha^n_{1/2}=0$ results in $\alpha^n_{M_n+1/2}=0$ per Equation 31 and the conservation equation is satisfied.

A relationship between $I_{m,n}$, $I_{m+1/2,n}$, and $I_{m-1/2,n}$ must be established. A weighted diamond difference scheme has been established by Morel and Montry [17],

$$I_{m,n}(r,z)=\tau_{m,n}I_{m+1/2,n}+(1-\tau_{m,n})I_{m-1/2,n}\quad(32)$$

where $\tau_{m,n}$ linearly interpolates μ:

$$\tau_{m,n} = \frac{\mu_{m,n} - \mu_{m-1/2,n}}{\mu_{m+1/2,n} - \mu_{m-1/2,n}} \tag{33}$$

with

$$\mu_{m+1/2,n} = \sqrt{1 - \xi_n^2} \cos\left(\varphi_{m+1/2,n}\right) \tag{34}$$

$$\varphi_{m+1/2,n} = \varphi_{m-1/2,n} + \pi \frac{w_{m,n}}{w_n} \tag{35}$$

$$w_n = \sum_{m=1}^{M_n} w_{m,n} \tag{36}$$

To incorporate reflecting boundary conditions, we will "guess" the incident angular fluxes, update them with outgoing angular fluxes from the previous iteration, and adapt a convergence criterion for those fluxes. Along the z-axis, the reflection for direction $\boldsymbol{\Omega} = (\mu, \eta, \xi)$ is $\boldsymbol{\Omega}_R = (-\mu, \eta, \xi)$.

5.2   Lumping

5.3   DSA

5.4   Symmetry Preservation

5.5   Other

6   Conclusions

6.1   FutureWork

Future work beyond the scope of these research objectives could include methods for solving the system of equations. Currently we simultaneously solve for every degree of freedom in the problem. This limits the overall number of unknowns that we can accommodate because they all get stored in memory. However, if we solved individual mesh cells and systematically "swept through the mesh" (solve the sparse system of equations for each quadrature direction, in parallel or sequentially), we eliminate this limitation. This allows for cycles (discussed in Section **??**) in the mesh, which require careful handling.

Negative energy densities, observed in some of the test problems above, may contribute to negative mass densities in the equations of state of multiphysics problems. This must be addressed. Mentioned previously are lumping the matrices that constitute the bilinear form or perform a negative energy density fix up. The latter results in a nonlinear system of equations, which may be satisfactory given the TRT equations are already nonlinear. Oscillations could be reduced by using lower order elements in susceptible regions. Investigating an adaptive element could prove beneficial.

Coupling the TRT equations with the hydrodynamics equations is a logical progression toward modeling a realistic problem. Understanding the coupling between equations may be challenging given the variety of physical phenomena in these problems. The increase in the number of degrees of freedom upon this coupling begs for an increase in efficiency. An investigation into increased parallelization is warranted along with solution methods such as sweeping through the mesh.

References

[1] John Castor. *Radiation Hydrodynamics*. Cambridge, 2007.

[2] R. Paul Drake. High-energy-density physics. *Physics Today*, 63(3):8–9, June 2010.

[3] Veselin A. Dobrev, Tzanio V. Kolev, and Robert N. Rieben. High-order curvilinear finite element methods for Lagrangian hydrodynamics. *SIAM Journal of Scientific Computing*, 34(5):B606 – B641, 2012.

[4] G. Scovazzi, E. Love, and M. J. Shashkov. Multi-scale Lagrangian shock hydrodynamics on Q1/P0 finite elements: Theoretical framework and two-dimensional computations. *Computer Methods in Applied Mechanics and Engineering*, 197:1056–1079, 2008.

[5] V. A. Dobrev, T. E. Ellis, Tz. V. Kolev, and R. N. Rieben. Curvilinear finite elements for lagrangian hydrodynamics. *International Journal for Numerical Methods in Fluids*, 2010.

[6] MFEM: Modular finite element methods. `mfem.org`, 2015.

[7] Thomas A. Brunner. Forms of approximate radiation transport. Technical report, Sandia National Laboratories, 2002.

[8] K. D. Lathrop and B. G. Carlson. Discrete ordinates angular quadrature of the neutron transport equation. Technical report, Los Alamos Scientific Laboratory of the University of California, 1965.

[9] Marvin L. Adams, Todd A. Wareing, and Wallace F. Walters. Characteristic methods in thick diffusive problems. *Nuclear Science and Engineering*, 130:18–46, 1998.

[10] E. E. Lewis and W. F. Miller, Jr. *Computational Methods of Neutron Transport*. American Nuclear Society, 1993.

[11] Edward W. Larsen and J. E. Morel. Asymptotic solutions of numerical transport problems in optically thick, diffusive regimes II. *Journal of Computational Physics*, 83:212–236, 1989.

[12] F. Malvagi and G. C. Pomraning. Initial and boundary conditions for diffusive linear transport problems. *Journal of Mathematical Physics*, 32(3):805–820, 1991.

[13] Edward W. Larsen. Unconditionally stable diffusion-synthetic acceleration methods for the slab geometry discrete ordinates equations. part I: Theory. *Nuclear Science and Engineering*, 82(1):47–63, 1982.

[14] Yaqi Wang and Jean C. Ragusa. Diffusion synthetic acceleration for high-order discontinuous finite element S_N transport schemes and application to locally refined unstructured meshes. *Nuclear Science and Engineering*, 166:145–166, 2010.

[15] Bruno Turcksin and Jean C. Ragusa. Discontinuous diffusion synthetic acceleration for S_N transport on 2D arbitrary polygonal meshes. *Journal of Computational Physics*, 274:356–369, 2014.

[16] Guido Kanschat. *Discontinuous Galerkin Methods for Viscous Incompressible Flow*. Deutscher Universit'ats-Verlag, 2007.

[17] J. E. Morel and G. R. Montry. Analysis and elimination of the discrete-ordinates flux dip. *Transport Theory and Statistical Physics*, 13(5):615–633, 1984.

[18] Marvin L. Adams. Discontinuous finite element transport solutions in thick diffusive problems. *Nuclear Science and Engineering*, 137(3):298–333, 2001.

[19] Douglas N. Woods, Thomas A. Brunner, and Todd S. Palmer. High order finite elements S_N transport in X-Y geometry on meshes with curved surfaces. *Transactions of the American Nuclear Society*, 114:377 – 380, June 2016.

A   Previous DSA Implementation

A.1   Varying Penalty within MFEM for Homogeneous Problems and/or Non-Uniform Meshes

The penalty term (Eq. 15) contains information from the problem. However, as currently implemented, the penalty term is a constant multiplier. To ensure Equation 15 holds within MFEM, we must create a new integrator class based on `DGDiffusionIntegrator` to modify the penalty term according to each of the mesh boundaries. Equation 15 states that the minimum penalty value is $1/4$, thus,

$$\kappa_{\text{MFEM}} \left\langle \left\{\!\left\{ \frac{D}{h_\perp} \right\}\!\right\} [\![\phi]\!], [\![w]\!] \right\rangle \equiv \kappa_e \left\langle [\![\phi]\!], [\![w]\!] \right\rangle \tag{37}$$

$$\kappa_{\text{MFEM}} \left\{\!\left\{ \frac{D}{h_\perp} \right\}\!\right\} \equiv \kappa_e \geq \frac{1}{4} \tag{38}$$

$$\kappa_{\text{MFEM}} \geq \frac{1}{4} \left\{\!\left\{ \frac{h_\perp}{D} \right\}\!\right\} \tag{39}$$

Thus, enforcing $\kappa_e = 1/4$, `DGDiffusionIntegrator` would become

$$\frac{1}{4} \left\{\!\left\{ \frac{h_\perp}{D} \right\}\!\right\} \left\langle \left\{\!\left\{ \frac{D}{h_\perp} \right\}\!\right\} [\![\phi]\!], [\![w]\!] \right\rangle \tag{40}$$

This method would effectively remove any user input to this integrator, determining the penalty coefficient internally. However, it fixes the penalty value $\kappa_e = 1/4$ rather than $\kappa_e = \max\left(\kappa_e^{IP}, 1/4\right)$. To fully adapt the MIP equations, the maximum $\kappa_e = \max\left(\kappa_e^{IP}, \kappa_{\text{MFEM}}\right)$ should be used where κ_e^{IP} is defined by Equation 14.

B   Older DSA Results

B.1   Diffusion Synthetic Acceleration

Results using the MIP DSA equations using Dirichlet boundary conditions (Eqs. 9 and 10) are solved and some results are compared to unaccelerated solutions in Table 1. The "Adams problem" is defined in Adams [18]. It is a homogeneous 2-D diffusion limit problem with Dirichlet boundary conditions. For the various values of ϵ shown, $\sigma_t = \epsilon^{-1}$, $\sigma_a = \epsilon$, $\sigma_s = \sigma_t - \sigma_a$, and $S_0 = \epsilon$. The Adams problem was discretized with 8th order finite elements, S_8 angular quadrature, and 8th order mesh. Convergence criteria $\epsilon_{\text{conv}} = 10^{-12}$ was used. The penalty term κ^{IP} was not determined exactly the same as [14]. Rather, an ad hoc value was used in order to assure convergence. This is the reason for increasing κ^{IP} as ϵ decreases.

The results shown in Table 1 are varied. As we increase the optical thickness of the problem, we were able to converge toward a solution in a much more reasonable

Table 1: "Adams" 2-D diffusion limit problem L^2 error between our solution and the reference solution for several values of ϵ. Note 1: did not attempt. Note 2: did not run to convergence. Note 3: converges consistently until some (seemingly arbitrary) point, then becomes erratic.

	without DSA		with DSA			
ϵ	spectral radius	no. iters	no. iters	spectral radius	κ^{IP}	L^2 error
0.1	0.94	474	44	0.53	10^2	0.048
0.05	0.98	1662	note 1	note 1	note 1	0.024
0.01	0.9993	$> 10,000$	49	0.56	10^2	0.0049
10^{-3}	0.9999	$> 10,000$	91 / > 91	0.76 / 0.81	10^3 / 10^4	0.00049
10^{-4}	note 1	note 1	note 2 / note 2 / note 2	0.66 (note 3) / 0.92 / 0.95	10^3 / 10^4 / 10^5	0.000049
10^{-5}	note 1	note 1	n/a / note 2	> 1 / 0.70 (note 3)	10^3 / 10^4	0.0000049
10^{-6}	note 1	note 1	n/a / note 2	> 1 / 0.70 (note 3)	10^4 / 10^5	0.000012

time with DSA than without. Thus, we have observed that we have the diffusion limit. However, this is not without some issues.

During the solution to the Adams problem using DSA for $\epsilon = \{10^{-4}, 10^{-5}, 10^{-6}\}$, the DSA solution was observed to evolve smoothly until it reached a (seemingly arbitrary) point when it begins to behave erratically. The erratic DSA solutions don't begin affecting the scalar flux solution until the magnitude of the DSA solution is on the same order as the maximum scalar flux error between iterations ($O\left(10^{-11}\right)$). Thus, the solutions to this problem for $\epsilon = \{10^{-4}, 10^{-5}, 10^{-6}\}$ are not fully converged. An example output is shown in Figure 2 to demonstrate that the spectral radius became erratic. This example is for $\epsilon = 10^{-4}$ where the spectral radius was consistently about 0.66 until iteration 51.

```
Itr = 50, phi_conv.max =   6.4492988e-11, spectral radius: 0.65659991
L2 error: 4.8937733e-05
Itr = 51, phi_conv.max =   5.7443356e-11, spectral radius: 0.89069149
L2 error: 4.8937729e-05
Itr = 52, phi_conv.max =   4.2847809e-11, spectral radius: 0.7459141
L2 error: 4.893773e-05
Itr = 53, phi_conv.max =   3.8060055e-11, spectral radius: 0.88826141
L2 error: 4.8937731e-05
Itr = 54, phi_conv.max =   2.6113472e-11, spectral radius: 0.68611231
L2 error: 4.8937738e-05
Itr = 55, phi_conv.max =   5.4752064e-11, spectral radius: 2.0966979
L2 error: 4.8937731e-05
Itr = 56, phi_conv.max =   5.4592192e-11, spectral radius: 0.99708007
L2 error: 4.8937735e-05
Itr = 57, phi_conv.max =   2.9092062e-11, spectral radius: 0.53289786
L2 error: 4.8937709e-05
Itr = 58, phi_conv.max =   7.1939399e-11, spectral radius: 2.4728188
L2 error: 4.8937725e-05
Itr = 59, phi_conv.max =   6.8166972e-11, spectral radius: 0.94756105
L2 error: 4.893773e-05
Itr = 60, phi_conv.max =   5.9108274e-11, spectral radius: 0.86711016
■
```

Figure 2: Partial output for Adams problem showing iteration number (Itr), maximum flux error between iterations (phi_conv.max), spectral radius, and the L^2 error from the reference solution.

The next set of test problems are for a uniform infinite medium using Dirichlet boundary MIP DSA with a zero analytic solution (incidentally it is equivalent the the Adams problem just with a zero volumetric source term). Specifically, $\sigma_t = 1/\epsilon$, $\sigma_a = \epsilon$, $S = 0$, $\psi_{\text{inc}} = 0$, and analytic solution $\phi = S/\sigma_a = 0.0$. The source iteration begins with an initial guess of $\phi = 5$. This problem was discretized with 8th order finite elements, S_8 angular quadrature, and 8th order mesh. Convergence criteria $\epsilon_{\text{conv}} = 10^{-12}$ was used. Table 2 illustrates various solution properties of these test problems.

The erratic behavior is not observed in this problem. As seen in Figures 3 and 4, the scalar flux and DSA solutions, respectively, show values on the order of 10^{-20}, far beyond the point that the DSA began behaving erratically. This suggests a discrepancy associated with the volumetric source term.

Table 2: 2-D uniform infinite medium diffusion limit problem L^2 error between our solution and the reference solution for several values of ϵ.

ϵ	no. iters	spectral radius	κ^{IP}	L^2 error
0.1	47	0.53	10^3	2.5×10^{-13}
0.01	51	0.56	10^3	3.4×10^{-13}
10^{-3}	104	0.76	10^3	1.6×10^{-13}
10^{-4}	70	0.66	10^3	6.0×10^{-14}
10^{-5}	n/a — 81	> 1 — 0.70	10^3 — 10^4	n/a — 7.4×10^{-14}
10^{-6}	n/a — 83	> 1 — 0.70	10^4 — 10^5	n/a — 6.0×10^{-14}
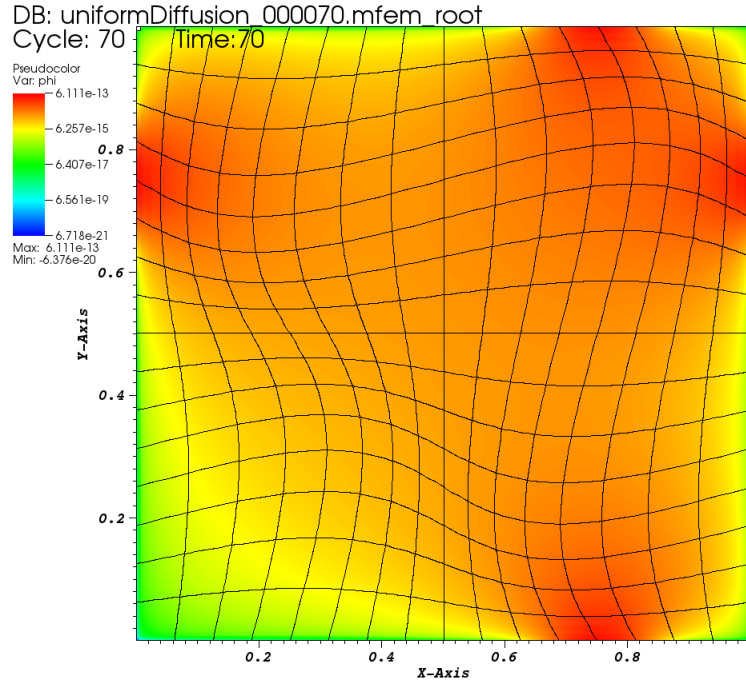
Figure 3: Uniform infinite medium diffusion limit scalar flux solution (log scale) for $\epsilon = 10^{-4}$ of Table 2.
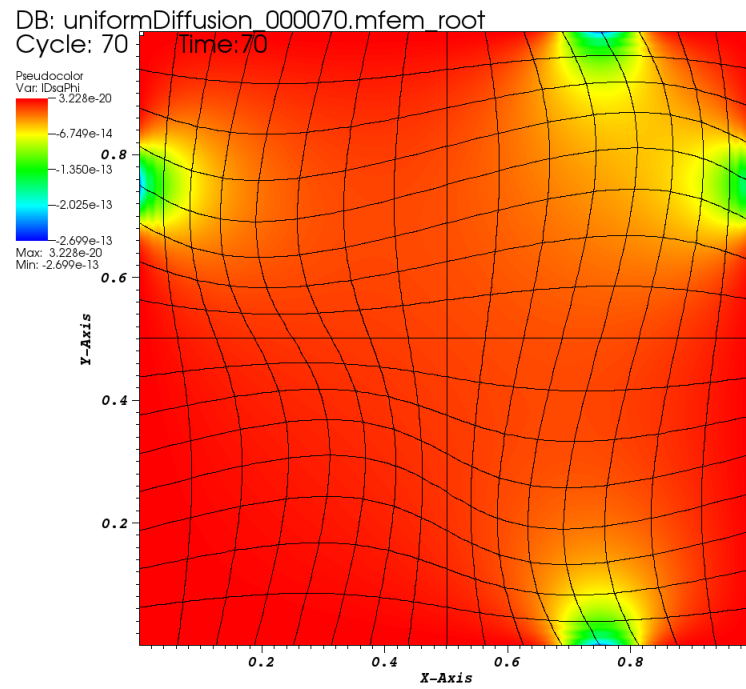
Figure 4: Uniform infinite medium diffusion limit DSA solution for $\epsilon = 10^{-4}$ of Table 2.

B.1.1   Strong Scatter with Discontinuous Boundary Conditions with DSA

This test problem was solved without DSA in Woods et al. [19]. Implementing the Dirichlet boundary condition DSA reduced the number of source iterations to 37 ($\rho \approx 0.54$) using $\kappa_{\text{MFEM}} = 1/2 \cdot h_\perp/D = 150$ where $h_\perp = \{0.1, 0.02\}$. The modified convergence criteria was used where $\epsilon_{\text{conv}} = 10^{-12}$. Figures 5 and 6 illustrate the solution and the natural log of the solution, respectively. This problem did not display any erratic convergence behavior.
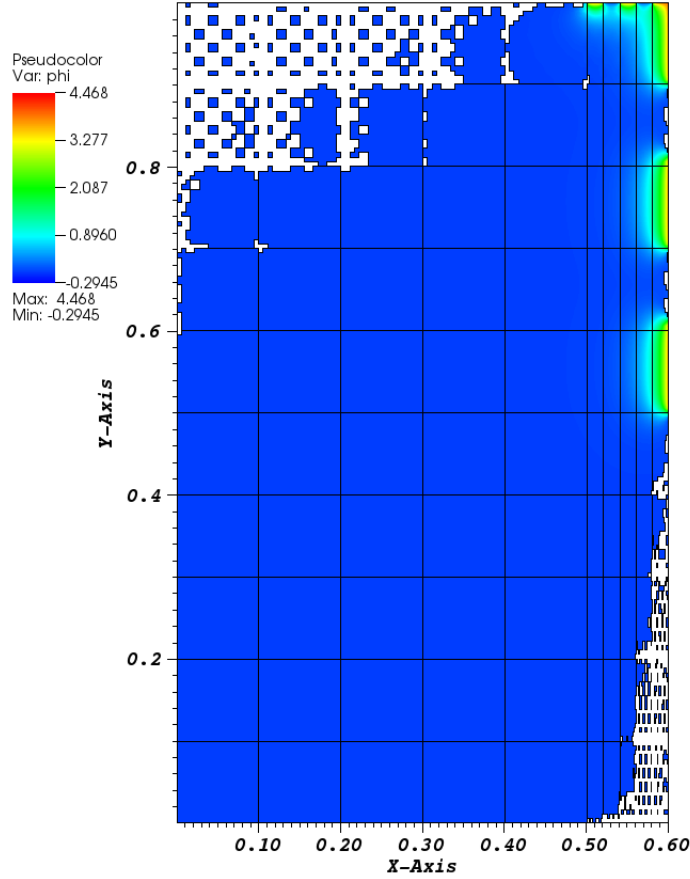

Figure 5: Strong scatter with discontinuous boundary conditions problem solved with DSA. White regions indicate negative fluxes.
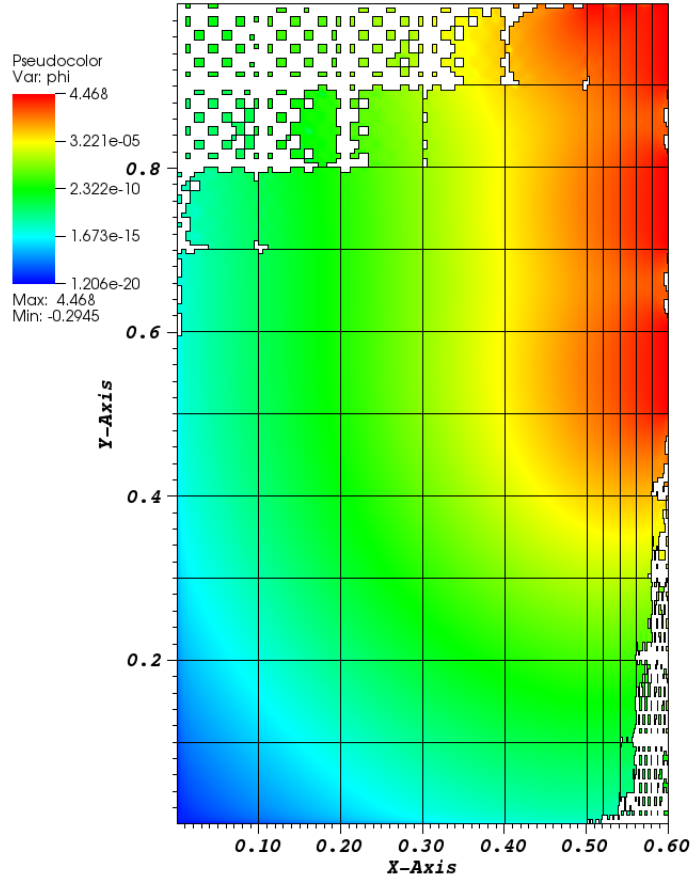
Figure 6: Log of strong scatter with discontinuous boundary conditions problem solved with DSA. White regions indicate negative fluxes.

B.1.2 Material Discontinuity Stress Test with DSA

Adding DSA to the material discontinuity stress test of Woods et al. [19] reduces the spectral radius to $\rho \approx 0.994$ using $\kappa_{\text{MFEM}} = 450$. A discussion of κ_{MFEM} is necessary. Both $\kappa_{\text{MFEM}} = 400$ and $\kappa_{\text{MFEM}} = 500$ caused the source iteration to diverge. This parameter is supposed to vary based on $h_{\perp}^{\pm}$ and $D^{\pm}$. Homogeneous problems on a regular mesh can have a global κ_{MFEM} but this heterogeneous problem will require multiple κ_{MFEM} values at the various material interfaces. For now, this global value allows the source iteration to converge and is still much faster than without DSA altogether.

This problem was solved using S_4 level-symmetric quadrature and 8th order finite elements. The modified convergence criteria was used where $\epsilon_{\text{conv}} = 10^{-12}$. An error occurred causing the calculation to stop every 900 iterations (about 55 minutes). Restarting the simulation from a restart file allowed this problem to converge according to the convergence criteria. This problem converged in 4027 iterations. Figures 7 and 8 illustrate the scalar flux solution and the log of the scalar flux, respectively.
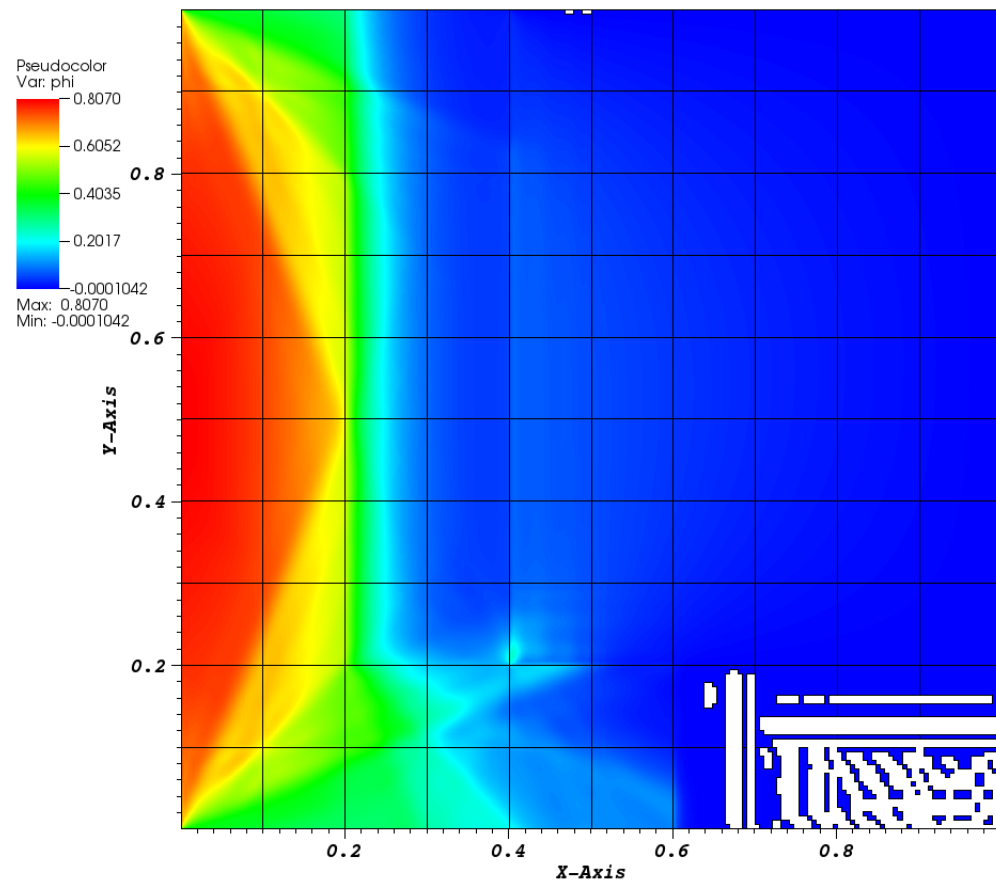
Figure 7: Material discontinuity stress test solved with DSA. White regions indicate negative fluxes.
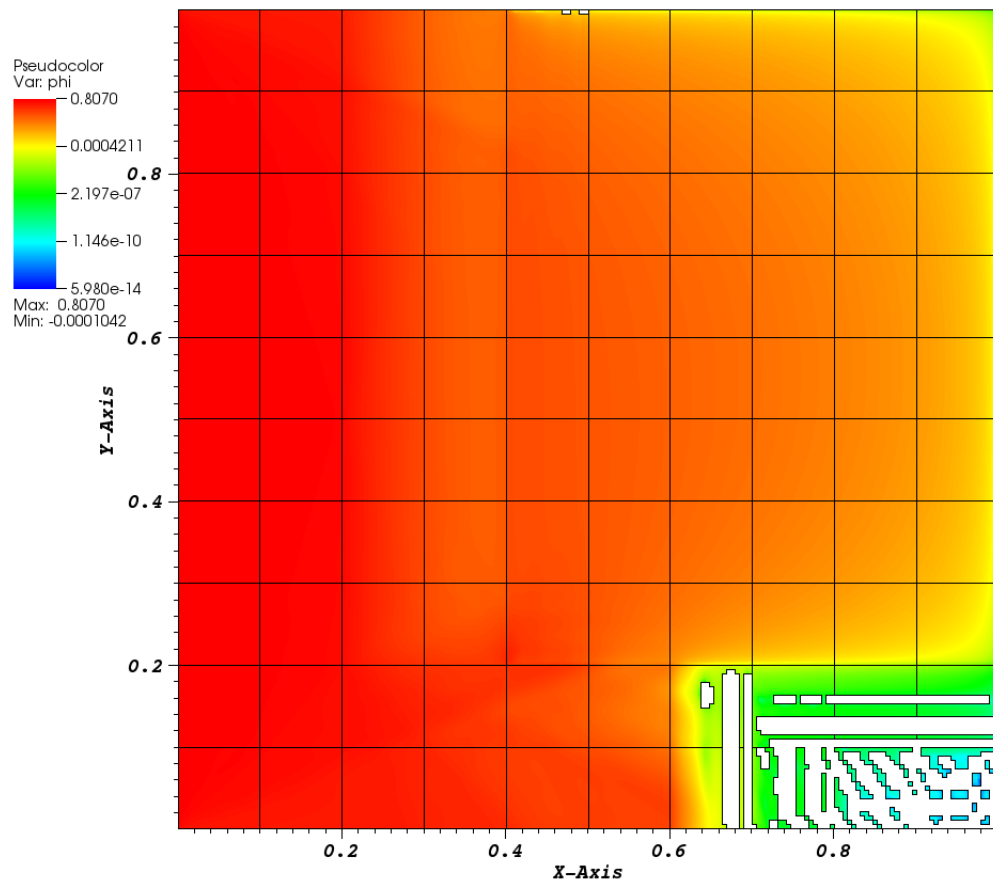
Figure 8: Log of material discontinuity stress test solved with DSA. White regions indicate negative fluxes.

This problem converged in significantly more iterations than the other test problems described above. Figure 9 illustrates the magnitude of the error between two successive iterations of scalar flux. Clearly, the slowest region to converge is within the highly scattering region near the very low and very high absorption regions.
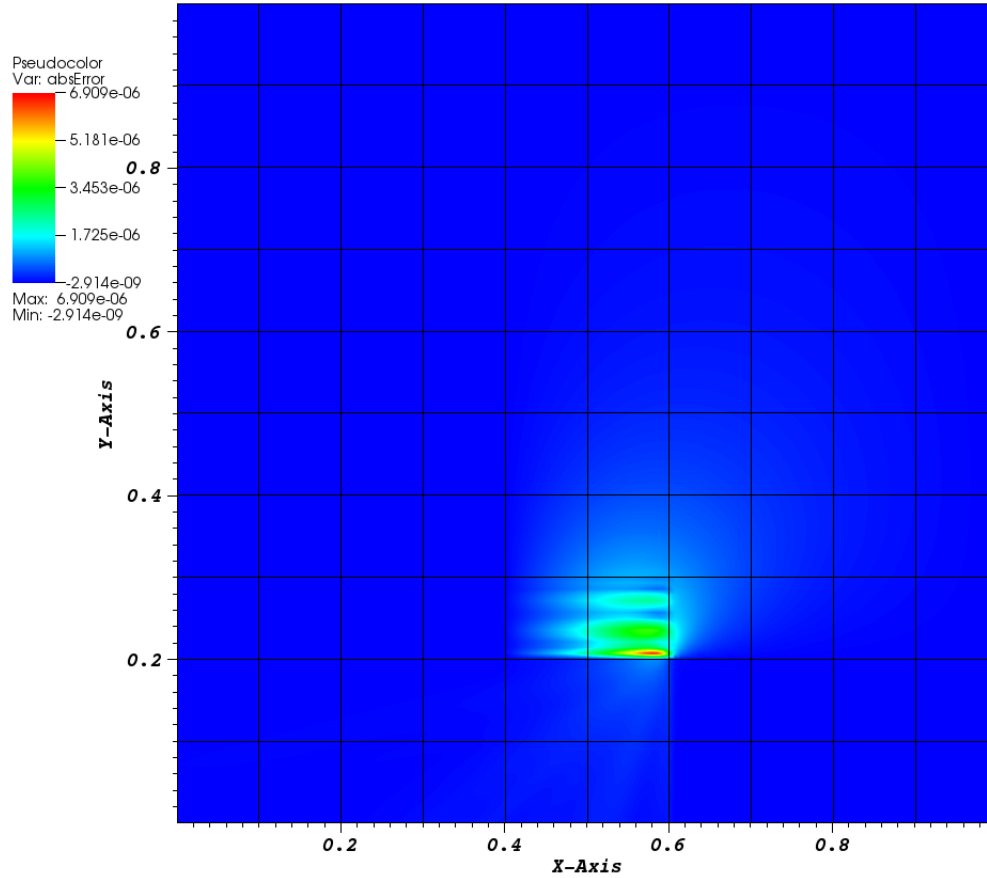

Figure 9: Magnitude of scalar flux error between successive iterations for material discontinuity stress test. This calculation was performed with S_8 level-symmetric quadrature.

C   Implementation in MFEM

C.1   MIP DSA

There are some specific function calls to MFEM for the diffusion equation that are listed in Table 3. Items 3 and 4 have a σ_D value that controls the DG method to be used, where $\sigma_D = -1$ is for the symmetric interior penalty method. Item 6 is for the Robin boundary condition described by Equation 18. Item 4 is the function that will need to be modified to adapt Methods 1 and 2 (this function is not used for Method 3).

no.	FEM Equations 9 & 10	MFEM Equation	User Input
1	$(\sigma_a\phi, w)_{\mathbb{V}}$	$(\sigma_a\phi, w)_{\mathbb{V}}$	MassIntegrator(σ_a)
2	$(D\boldsymbol{\nabla}\phi, \boldsymbol{\nabla} w)_{\mathbb{V}}$	$(D\boldsymbol{\nabla}\phi, \boldsymbol{\nabla} w)_{\mathbb{V}}$	DiffusionIntegrator(D)
3	$(\{\!\{D\partial_n\phi\}\!\}, [\![w]\!])_{\partial\mathbb{V}^i}$ $+([\![\phi]\!], \{\!\{D\partial_n w\}\!\})_{\partial\mathbb{V}^i}$ $+(\kappa_e[\![\phi]\!], [\![w]\!])_{\partial\mathbb{V}^i}$	$(\{\!\{D\boldsymbol{\nabla}\phi\cdot\hat{n}\}\!\}, [\![w]\!])_{\partial\mathbb{V}^i}$ $+\sigma_D([\![\phi]\!], \{\!\{D\boldsymbol{\nabla} w\cdot\hat{n}\}\!\})_{\partial\mathbb{V}^i}$ $+\kappa\left(\{\!\{\frac{D}{h_\perp}\}\!\}[\![\phi]\!], [\![w]\!]\right)_{\partial\mathbb{V}^i}$	DGDiffusionIntegrator(D, σ_D, κ)
4	$(\{\!\{D\partial_n\phi\}\!\}, [\![w]\!])_{\partial\mathbb{V}^d}$ $-\frac{1}{2}([\![\phi]\!], \{\!\{D\partial_n w\}\!\})_{\partial\mathbb{V}^d}$ $-\frac{1}{2}(\kappa_e[\![\phi]\!], [\![w]\!])_{\partial\mathbb{V}^d}$	$(\{\!\{D\boldsymbol{\nabla}\phi\cdot\hat{n}\}\!\}, [\![w]\!])_{\partial\mathbb{V}^d}$ $+\sigma_D([\![\phi]\!], \{\!\{D\boldsymbol{\nabla} w\cdot\hat{n}\}\!\})_{\partial\mathbb{V}^d}$ $+\kappa\left(\{\!\{\frac{D}{h_\perp}\}\!\}[\![\phi]\!], [\![w]\!]\right)_{\partial\mathbb{V}^d}$	DGDiffusionIntegrator(D, σ_D, κ)
5	$(Q_0, w)_{\mathbb{V}}$	$(Q_0, w)_{\mathbb{V}}$	DomainLFIntegrator(Q_0)
6	$(\frac{1}{2}\phi, w)_{\partial\mathbb{V}^d}$	$(\frac{1}{2}\phi, w)_{\partial\mathbb{V}^d}$	BoundaryMassIntegrator($\frac{1}{2}$)

† $\partial\mathbb{V}^i$ denotes an internal edge
‡ $\partial\mathbb{V}^d$ denotes a boundary edge

Table 3: MFEM diffusion equation function calls.

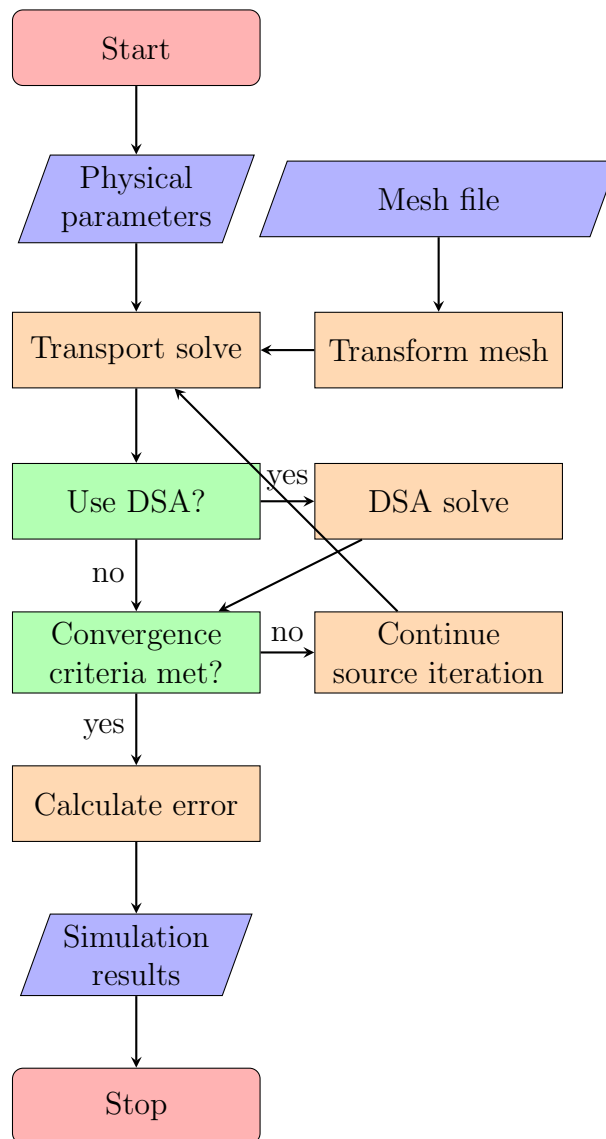Figure 10: Flow diagram for solution process.

D   Mesh Examples